

# Mixing across fluid interfaces compressed by convective flow in porous media

Juan J. Hidalgo<sup>1,2</sup> & Marco Dentz<sup>1,2</sup>

<sup>1</sup> IDAEA-CSIC, Barcelona, 08034, Spain

<sup>2</sup> Associated Unit: Hydrogeology Group (UPC-CSIC), Barcelona, Spain

January 16, 2022

## Abstract

We study the mixing in the presence of convective flow in a porous medium. Convection is characterized by the formation of vortices and stagnation points, where the fluid interface is stretched and compressed enhancing mixing. We analyze the behavior of the mixing dynamics in different scenarios using an interface deformation model. We show that the scalar dissipation rate, which is related to the dissolution fluxes, is controlled by interfacial processes, specifically the equilibrium between interface compression and diffusion, which depends on the flow field configuration. We consider different scenarios of increasing complexity. First, we analyze a double-gyre synthetic velocity field. Second, a Rayleigh-Bénard instability (the Horton-Rogers-Lapwood problem), in which stagnation points are located at a fixed interface. This system experiences a transition from a diffusion controlled mixing to a chaotic convection as the Rayleigh number increases. Finally, a Rayleigh-Taylor instability with a moving interface, in which mixing undergoes three different regimes: diffusive, convection dominated, and convection shutdown. The interface compression model correctly predicts the behavior of the systems. It shows how the dependency of the compression rate on diffusion explains the change in the scaling behavior of the scalar dissipation rate. The model indicates that the interaction between stagnation points and the correlation structure of the velocity field is also responsible for the transition between regimes. We also show the difference in behavior between the dissolution fluxes and the mixing state of the systems. We observe that while the dissolution flux decreases with the Rayleigh number, the system becomes more homogeneous. That is, mixing is enhanced by reducing diffusion. This observation is explained by the effect of the instability patterns.

## 1 Introduction

Convective flow caused by an unstable stratification of fluid density such as the Rayleigh-Bénard or the Rayleigh-Taylor instabilities are common in porous media. The Rayleigh-Bénard instability appears when an unstable density stratification is maintained between the top and bottom boundaries of the domain. This is often found when the fluid temperature is altered as in geothermal groundwater systems (Cheng, 1979; Sanford et al., 1998) and heat conduction in metallic foams (Dyga and Troniewski, 2015; Hamadouche et al., 2016), or during the mixing of freshwater and seawater in coastal aquifers (Cooper, 1964; Abarca et al., 2007). The Rayleigh-Taylor instability occurs when one fluid is placed on top of a less dense one. A situation found in geological

CO<sub>2</sub> storage (Ennis-King and Paterson, 2005; Szulczewski et al., 2013), the displacement of dense contaminant plumes (Kueper and Frind, 1991), or the convection of compositional melts (Martin et al., 1987; Tait and Jaupart, 1989; Wells et al., 2011). The coupling between flow and transport results in an enhancement of boundary and dissolution fluxes and fluid mixing. Since mixing leads to the attenuation of concentration contrasts and dilution (Kitanidis, 1994; Dentz et al., 2011; Le Borgne et al., 2015) and drives chemical reactions (De Simoni et al., 2005; Dentz et al., 2011), understanding how unstable flow and mixing interact is therefore essential to predict the behavior of such systems.

The behavior of mixing and dissolution fluxes is usually expressed in terms of dimensionless quantities. In Rayleigh-Bénard instabilities, the fluxes are represented by the Nusselt number  $Nu$  (see Otero et al., 2004) and depend on the strength of the instability given by the Rayleigh number  $Ra$ . The numerical simulations of Otero et al. (2004) found  $Nu \propto Ra^{0.9}$  for  $1300 \lesssim Ra \lesssim 10000$ ; Hewitt et al. (2012) found exponents close to 1 for  $Ra > 1000$ . These observations are in agreement with the boundary layer analysis of Howard (1966) that assumes that the buoyancy flux is independent of the height of the domain. Although the low  $Ra$  regime is not discussed, inspection of Figure 3 in Otero et al. (2004) and Figure 2 in Hewitt et al. (2012) shows that  $Nu \propto Ra^{1/2}$  for  $100 \lesssim Ra \lesssim 1000$ , which differs from the  $Nu \propto Ra^{2/3}$  predicted by Kimura et al. (1986).

Rayleigh-Taylor instabilities also display different scaling depending on the dominant mechanism (Slim, 2014). The system evolves from  $Nu \propto Ra^{1/2}$  when diffusion dominates to  $Nu \propto Ra$  after the onset of the instabilities (Hidalgo et al., 2012, 2015). In bounded domains, as the instabilities attenuate, the relation between  $Nu$  and  $Ra$  becomes time dependent (Hewitt et al., 2013a; Hidalgo et al., 2015).

We focus on the behavior of dissolution fluxes, and fluid mixing in the presence of convective flow. Mixing in unstable systems occurs at the fluid interfaces that be located at the domain boundaries or at another and whose shape is determined by the instability patterns. The patterns organize themselves into cells, columnar plumes, or fingers, and evolve jointly with the velocity field, which forms vortices and stagnation points. The fluid interface is stretched and compressed at these locations, especially at stagnation points, affecting the magnitude of the fluxes across it.

We study the hydrodynamic mechanism of convective mixing and dissolution and quantify them in an interface compression model that is able to reproduce the observed mixing scaling. The model relates the structure of the velocity field to mixing and dissolution fluxes across the fluid interface. First, we present the governing equations of the flow and transport in porous media and define the observables that describe the system, namely, the scalar dissipation rate and concentration probability density function and discuss their relation to dissolution fluxes and mixing state of the system. Then we introduce the interface compression model for the mixing and dissolution fluxes in the vicinity of a stagnation point. We consider three scenarios with increasing complexity. A double-gyre synthetic velocity which is used to validate the interface compression model, a heat transport problem in which a Rayleigh-Bénard instability is triggered by the boundary conditions, and a two-fluid system in which the density stratification provokes a Rayleigh-Taylor instability. The interface compression models shows how mixing is controlled by the structure of the velocity field, whose properties determine the transition between scalings.

## 2 Flow and transport governing equations

Under the assumptions of incompressible fluids and the Boussinesq approximation, the dimensionless governing equations for variable-density single-phase flow in a 2D homogeneous porous medium are (Riaz et al., 2006; Hidalgo et al., 2013):

$$\nabla \cdot \mathbf{q} = 0, \quad (1)$$

$$\mathbf{q} = -\nabla p - \rho(c)\hat{\mathbf{e}}_g, \quad (2)$$

$$\frac{\partial c}{\partial t} + \mathbf{q} \cdot \nabla c - \frac{1}{\text{Ra}} \nabla^2 c = 0, \quad (3)$$

where  $p$  is a scaled pressure referred to a hydrostatic datum,  $\mathbf{q}$  is the dimensionless Darcy velocity, and  $\hat{\mathbf{e}}_g$  is a unit vector in the direction of gravity. The dimensionless density  $\rho$  is in general a function of concentration  $c$ . Choosing as time scale the advective characteristic time  $t_a = L_c/q_c\phi$ , where  $L_c$  is the system length scale,  $\phi$  the porosity, and  $q_c = k\rho_c g/\mu$  the characteristic buoyancy velocity given by the permeability  $k$ , viscosity  $\mu$ , a representative density  $\rho_c$ , and gravity  $g$ , the transport equation (3) is controlled only by the Rayleigh number

$$\text{Ra} = \frac{q_c L_c}{\phi D_m}, \quad (4)$$

where  $D_m$  is the diffusion coefficient. The different scales must be chosen depending on the problem solved and will be explained when necessary.

The system behavior is analyzed in terms of the global scalar dissipation rate

$$\langle \chi \rangle = \frac{1}{\text{Ra}} \int_{\Omega} d\Omega |\nabla c|^2, \quad (5)$$

where  $\Omega$  denotes the domain. At the steady state,  $\langle \chi \rangle$  is equal to the flux through the boundaries (Hidalgo et al., 2012) and since  $\text{Nu}$  is defined as the that flux divided by the diffusive flux over the domain ( $1/\text{Ra}$  in the current setup), it can be seen that  $\langle \chi \rangle = \text{Nu}/\text{Ra}$ .

In closed systems the change of concentration variance (Le Borgne et al., 2010) is equal to  $2\langle \chi \rangle$ . As the system mixes and concentration homogenizes  $\langle \chi \rangle$  goes to zero. However, in the presence of sinks or sources the concentration variance is also related to the boundary or dissolution fluxes (Hidalgo et al., 2012). In that case a non-zero  $\langle \chi \rangle$  proportional to the fluxes can be found in the steady state. In that case the mixing state of the system is better represented by the probability density function (pdf) of the concentration calculated by sampling the concentration in all the domain as

$$p(c) = \frac{1}{A} \int_{\Omega} \delta[c - c(\mathbf{x})] d\Omega, \quad (6)$$

where  $A$  is the domain's area.

The shape of the  $p(c)$  when the system is well-mixed depends on the boundary conditions. For example, for a well-mixed closed system,  $p(c)$  is given by a Dirac delta centered at the average initial concentration. If Dirichlet boundary conditions maintain a concentration difference between the system's boundaries and diffusion is the only transport mechanisms the concentration profile is linear and the pdf flat. Segregated systems are characterized by broad concentration pdfs with multiple local maxima.

To obtain information about the the spatial structure we shall use the two-dimensional auto-correlation function

$$\text{ACF}_g(x, y) = \mathcal{F}^{-1} \left\{ |\mathcal{F}\{g(x, y)\}|^2 \right\}, \quad (7)$$

where  $g(x, y)$  whose autocorrelation is computed and  $\mathcal{F}$  stands for the two-dimensional Fourier transform. The shape of ACF indicates the presence of periodic structures. The correlation length  $l$  is related to the width of the first maximum of the ACF and gives information about the size of those structures.

### 3 Interface compression

After the onset of instabilities, the fluid interface evolves under the combined effect of velocity and diffusion (Elder, 1968). In the locations where the velocity field experiences sharp changes, such as the stagnation points where the flow velocity goes to zero over a distance equal to the interface thickness, the interface is compressed and stretched. Diffusion, however, has the opposite effect and wants to increase the interface width. The thickness  $s$  of the interfacial boundary layer thus is the result of the competition between hydrodynamic compression and diffusive expansion, which can be quantified by (Villermaux, 2012; Le Borgne et al., 2013)

$$\frac{1}{s} \frac{ds}{dt} = -\gamma + \frac{1}{\text{Ra}} \frac{1}{s^2}, \quad (8)$$

with the dimensionless compression rate  $\gamma$ ; the dimensionless diffusion coefficient is  $\text{Ra}^{-1}$ . The compression rate is given by the symmetric part of the strain tensor (Ottino, 1989)

$$\mathbf{E} = \frac{1}{2}(\nabla \mathbf{q} + \nabla \mathbf{q}^T) = \begin{bmatrix} \gamma & 0 \\ 0 & -\gamma \end{bmatrix} \quad (9)$$

The steady state solution of (8) determines the length scale

$$s_B = \frac{1}{\sqrt{\gamma \text{Ra}}}, \quad (10)$$

at which the effects of compression and diffusion equilibrate. This length is known as the Batchelor scale (Batchelor, 1959; Villermaux and Duplat, 2006).

In general the scalar transport in the vicinity of a stagnation point located at a fluid interface can be described by the advection-diffusion equation (Ranz, 1979; Villermaux, 2012; Le Borgne et al., 2013; Hidalgo et al., 2015)

$$\frac{\partial c}{\partial t} = \gamma z \frac{\partial c}{\partial z} + \frac{1}{\text{Ra}} \frac{\partial^2 c}{\partial z^2}, \quad (11)$$

where horizontal gradients are disregarded because they are small along the interface and the stagnation point is located at  $z = 0$ . Following Hidalgo et al. (2015), the steady state solution for  $c$  along its characteristics gives

$$c = c_b + \frac{1 - c_b}{2} \text{erfc} \left( \frac{z}{\sqrt{2s_B^2}} \right), \quad (12)$$

where it is considered that the concentration far above the interface ( $z \rightarrow -\infty$ ) is 1 and far below the interface ( $z \rightarrow \infty$ ) has a value  $c_b$ , which can be different from zero

Using (12) in (5) we obtain the expression for  $\langle \chi \rangle$

$$\langle \chi \rangle = \frac{\omega_e}{\sqrt{4\pi}} \frac{(1 - c_b)^2}{s_B \text{Ra}}, \quad (13)$$

where  $\omega_e$  denotes an effective interface length in the horizontal direction. The form of  $\omega_e$  depends on the characteristics of the flow and will be discussed for each of the considered scenarios.

## 4 Mixing around a stagnation point: the double-gyre

To illustrate the interface compression model we analyze the behavior of fluxes and mixing using a double-gyre velocity field (Shadden et al., 2005). This is a simplified model of convective flow, because flow and transport are uncoupled, and flow around stagnation points. Similar models have been used to characterize mixing in oceanic circulation (Musgrave, 1985).

### 4.1 Double-gyre

We consider a rectangular domain of length 2 and height 1 in which the incompressible velocity  $\mathbf{q} = (q_x, q_z)$  is given by

$$q_x = \sin(n\pi x) \cos(\pi z)/n \quad (14)$$

$$q_z = -\cos(n\pi x) \sin(\pi z), \quad (15)$$

where  $n$  is a positive integer equal to 1 for the double-gyre. Concentration is prescribed on top and bottom boundaries so that

$$c(x, z) = \begin{cases} 0 & \text{at } z = 0 \\ 1 & \text{at } z = 1 \end{cases} \quad (16)$$

and the lateral boundaries are periodic. Density is constant and flow and transport are not coupled. There is no characteristic buoyancy velocity, so we take  $q_c = \max(q_z) = 1$  and  $\text{Ra} = q_c L_c / \phi D_m$ , which is in fact a Péclet number since the velocity field is not related to convective instabilities.

### 4.2 Interface compression and scalar dissipation

The velocity field varies smoothly along the vertical direction and compresses the fluid against the top boundary and maintains the concentration gradient. The structure of the velocity field can also be visualized through the determinant of  $|\mathbf{E}|$ , which displays extremes at the stagnation points. The velocity 2D autocorrelation also reveals the periodicity of the velocity field (Figure 1).

There are eight stagnation points in the domain (Figure 1). At the steady state only the ones at the boundaries contribute to mixing because the concentration gradients inside the domain are zero. We take the one at the center of the top boundary where the interface is compressed for the calculations. The compression rate at that point is  $\gamma = \pi$  and (10) gives  $s_B = \sqrt{1/\pi \text{Ra}}$ . Therefore from (13) we obtain

$$\langle \chi \rangle \sim \frac{1}{2\sqrt{\text{Ra}}} \quad (17)$$

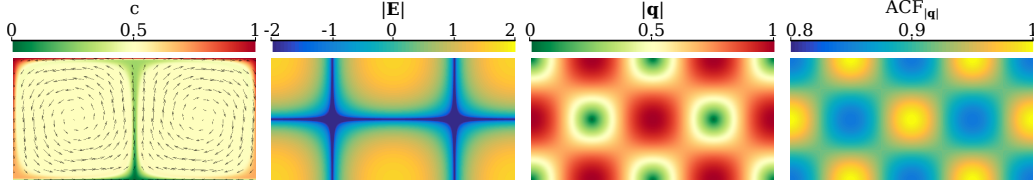


Figure 1: From left to right: steady state concentration and velocity field (arrows) for the double-gyre ( $Ra = 5000$ ), determinant of the strain tensor  $\mathbf{E}$ , magnitude of the velocity, and 2D normalized autocorrelation of the velocity field. The autocorrelation is computed using the Wiener-Khinchin Theorem and results are shifted so that the maximum is at the center of the domain.

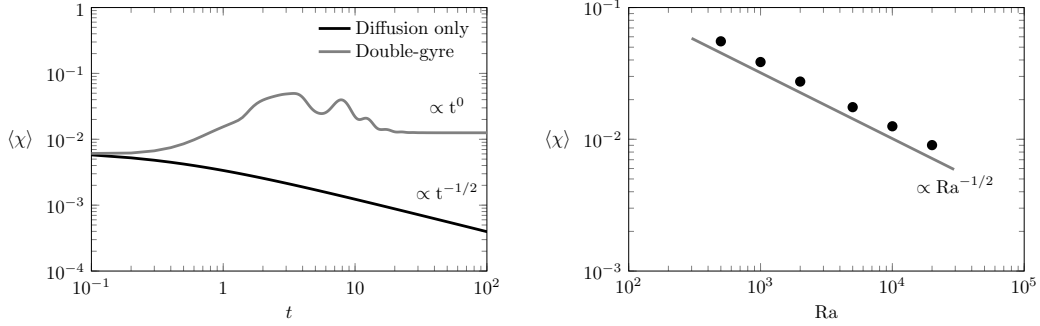


Figure 2: Left: Comparison between a diffusion only case (black solid line), that is velocity equal zero, and the case with a double gyre velocity field for  $Ra = 10000$  (gray solid line). The global scalar dissipation rate scales as  $t^{-1/2}$  for late times in the diffusion case while the double-gyre evolves to a constant behavior. Right: Dependence of the total mixing  $\langle \chi \rangle$  with  $Ra$  for the double gyre.

The  $Ra^{-1/2}$  dependence was observed by Ching and Lo (2001) for similar velocity fields. In the double gyre, the velocity changes in a scale of the order of the domain and  $\gamma$  is therefore independent of the value of  $Ra$ . Thus the  $Ra^{-1/2}$  behavior is characteristic of systems in which the velocity field (and  $\gamma$ ) and diffusion are uncoupled.

To verify the stagnation point model, we solved the double-gyre transport problem for  $500 < Ra < 20000$ . As expected, the effect of the convection increases the mixing efficiency of the system (Figure 2 left), which arrives to a steady state much faster than the only diffusion case. The global scalar dissipation rate displays the expected  $Ra^{-1/2}$  behavior (Figure 2 right).

As time passes the interface is compressed at the stagnation point until the compression of the velocity field is balanced by diffusion and the width equilibrates at the Batchelor scale  $s_B$ . The interface width can be estimated as the square root of the second central moment (variance) of  $c(1 - c)$  at the stagnation point as illustrated in Figure 3. There is a good agreement between the theoretical Batchelor scale and the numerical model (Figure 4).

The number of stagnation points and convection cells in the system increases with  $n$ . There are  $2n - 1$  convection cells and  $2n$  stagnation points where the interface is compressed. The compression rate at the stagnation points is independent of  $n$  and so is  $\max(q_z)$ . Therefore,  $Ra$  does not change. The simulations show that  $\langle \chi \rangle$  decreases with the number of cells (Figure 5 left). The decrease of

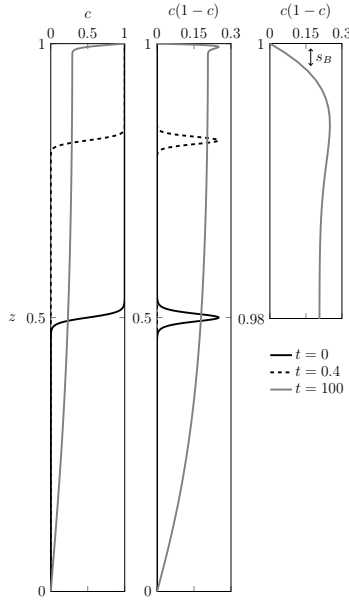


Figure 3: Concentration profile (left) and  $c(1-c)$  of the concentration (right) for the double gyre ( $n = 1$ ) at  $x = 0.5$  for times  $t = 0, 0.4, 100$ . It can be seen how the interface is compressed against the top and bottom boundary as the system approaches to the steady state. The decrease in the interface width is shown by the shape of  $c(1-c)$ .

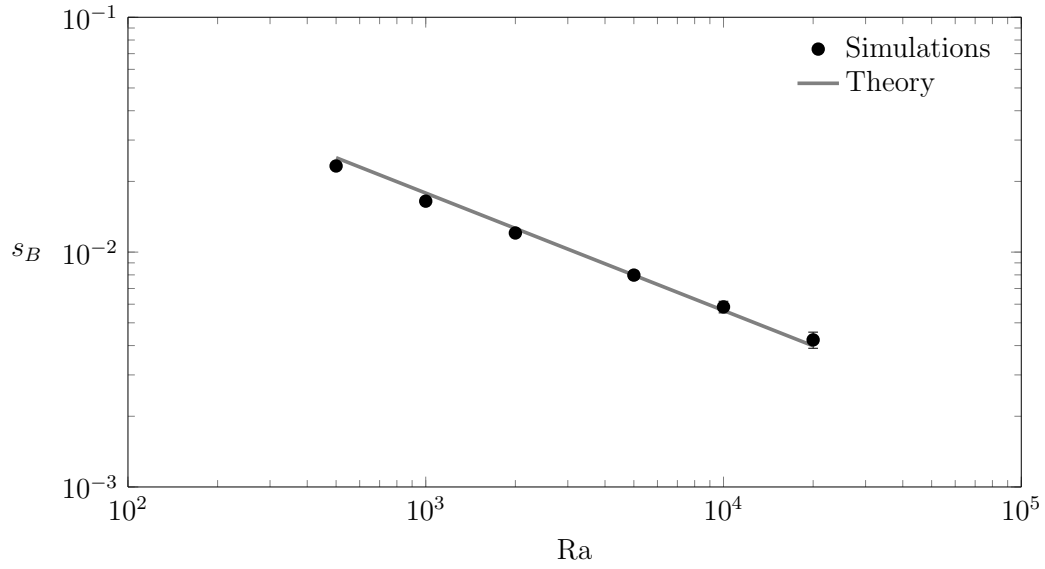


Figure 4: Computed (dots) interface width at the stagnation point and theoretical (solid line) Batchelor scale ( $s_B = (\pi Ra)^{-1/2}$ ).

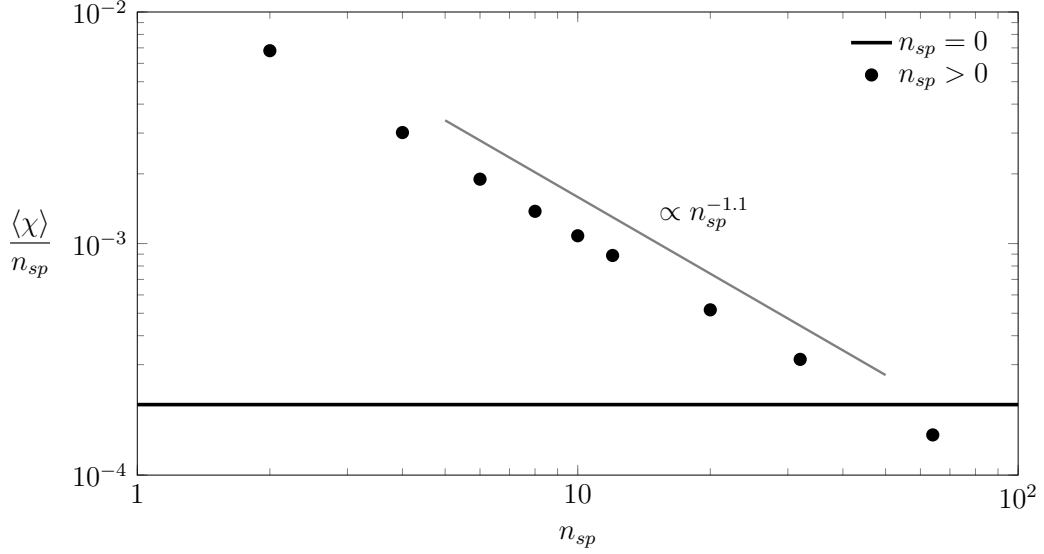


Figure 5: Global scalar dissipation rate with increasing number of stagnation points for  $Ra = 10000$ . The solid horizontal line corresponds to the case in which diffusion is the only transport mechanism ( $n_{sp} = 0$ ).

dissolution efficiency per stagnation point is caused by a reduction in the width of the cells. This reduction behaves as  $n^{-1}$  in good agreement with the numerical results.

### 4.3 Mixing state

The mixing state of the system is represented by the concentration pdf  $p(c)$  and its variance  $\sigma_c^2$  also show the effect of convection. Without convection the pdf (Figure 6 left) is uniform for all the concentration range because the concentration profile is linear. As  $Ra$  increases and the well-mixed area inside the convection cells grows and then concentration differences are confined near the boundaries. The weight of the extreme concentration decreases and the pdf sharpens around the mean value of 0.5. The peaks at  $c = 0$  and  $c = 1$  corresponding to the boundary conditions are always visible. The secondary peaks correspond to the areas around the stagnation points near the boundaries where the mean concentration is in between that of the boundary and the well-mixed zone inside the cells.

Convection also helps in making the system more homogeneous. When diffusion is the only mixing mechanism  $p(c)$  has the maximum variance possible because all values of concentration are equiprobable (Figure 6 right). The concentration variance  $\sigma_c^2$  is inversely proportional to  $Ra$  reflecting the above-mentioned reduction of the area occupied by concentration gradients.

The number of cells also affects the system state. The concentration pdf displays a sharper shape (Figure 7 left) and the number of secondary peaks increases with  $n$ . The stirring of additional convection cells, however, does not improve the homogeneity of the steady state system significantly. The variance of concentration (Figure 7 right) is not reduced significantly by the addition of more cells. It is interesting to note that the higher the dissolution flux, i.e. higher  $\langle \chi \rangle$ , the less well-mixed



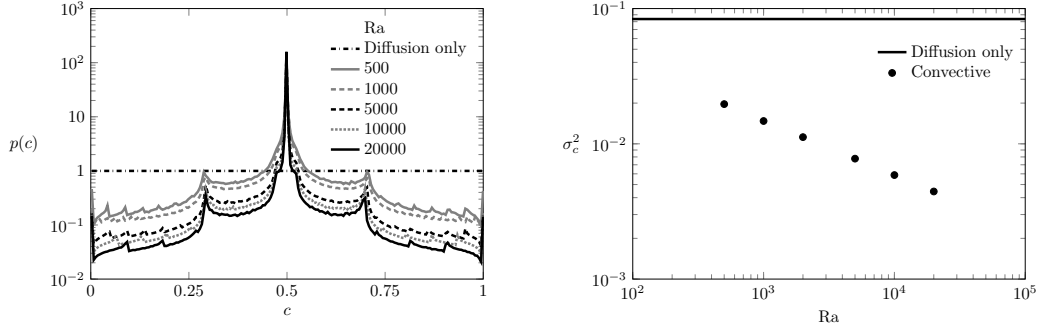


Figure 6: Steady state concentration pdf for the double-gyre case ( $n = 1$ ) and different values of  $Ra$  (left) and the pdf variance (right). The diffusion only case is computed with  $Ra = 10000$ .

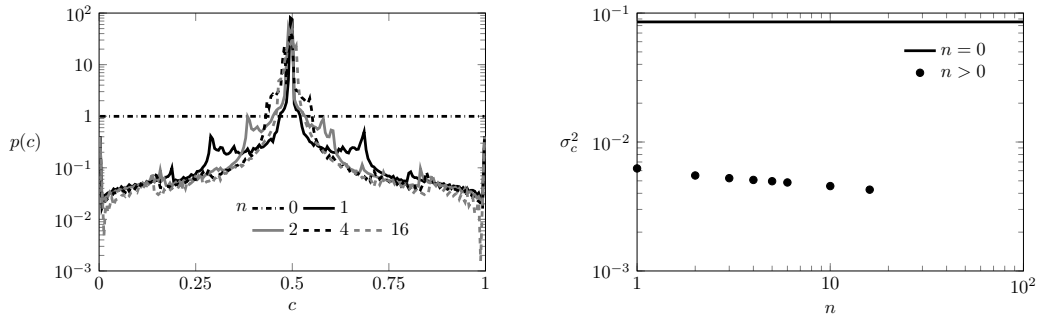


Figure 7: Concentration pdf (left) and variance (right) for multiple-gyre case for different values of  $n$  and  $Ra = 10000$ . The velocity field homogenizes the system. However, the efficiency above  $n = 1$  decreases significantly.

the system is.

## 5 Mixing across immobile interfaces

We consider now a system for which the instabilities originate at the boundary and propagate to the rest of the finite domain. The interface is then fixed on one side and the shape of the instability patterns is constrained in principle by the geometry of the system.

### 5.1 The Horton-Rogers-Lapwood problem

The Horton-Rogers-Lapwood (HRL) problem (Horton and Rogers, 1945; Lapwood, 1948) is a heat transport problem in which convection is triggered by a Rayleigh-Bénard instability caused by the temperature difference between the top and bottom boundaries. We solve the problem in a rectangular domain of aspect ratio 2 (as in the double-gyre case) with impervious top and bottom boundaries and periodic boundary conditions on the sides. Temperature  $T = 1$  is prescribed at the top boundary and  $T = 0$  at the bottom one. The dimensionless density of the fluid increases linearly

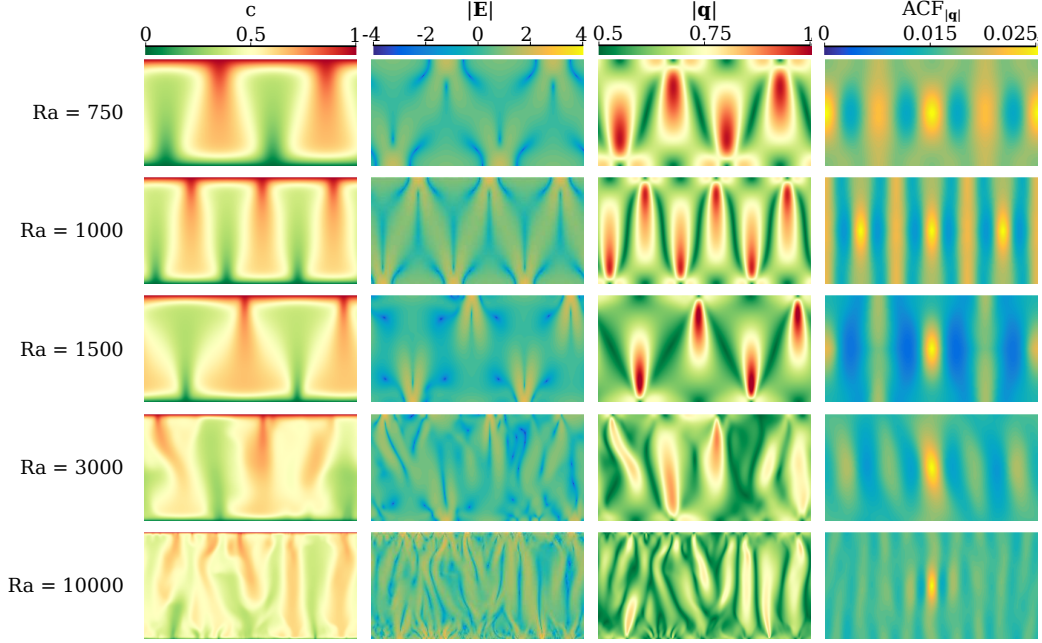


Figure 8: From left to right: concentration, determinant of the strain tensor  $\mathbf{E}$ , modulus of the velocity, and 2D normalized autocorrelation of the velocity field for the Horton-Rogers-Lapwood problem and different  $Ra$  at time  $t = 1000$ . The autocorrelation is computed using the Wiener-Khinchin Theorem and results are shifted so that the maximum is at the center of the domain.

with temperature as  $\rho = \beta T$ , where  $\beta$  is a positive constant. The system is again characterized by the Rayleigh number (4), which in this case takes the form  $Ra = k\beta L_c / \phi\mu D_m$  since  $q_c = k\beta/\mu$ .

The system is stable for  $Ra < 4\pi^2$ . For  $4\pi^2 \lesssim Ra \lesssim 1300$  (Graham and Steen, 1994) the instability patterns occupy the whole domain in the form of convection cells (Figure 8). For higher  $Ra$  the system evolves to a chaotic convection regime in which flow is organized in columnar patterns (Hewitt et al., 2013b). This transition occurs around  $Ra_c \sim 1300$ , which will be called critical Rayleigh number in the following.

The stagnation points in this problem are located at the top and bottom boundaries (Figure 8). For moderate  $Ra$  they are found in between the convection cells and remain stationary once the convection is fully developed. For high  $Ra$  when the system experiences chaotic convection, the stagnation points are located at the boundaries from where the columnar plumes grow. They appear and disappear along the boundary as the small proto-plumes merge and interact.

## 5.2 Interface compression and and scalar dissipation

The global scalar dissipation rate  $\langle \chi \rangle$  reflects the transition of the system from an uncoupled, self-organized, convective regime, in which  $\langle \chi \rangle \propto Ra^{-1/2}$  as in the double-gyre scenario, to a convection dominated regime characterized by  $\langle \chi \rangle \propto Ra^0$  (Figure 9). The origin of this change in the system's behavior lies in the structure of the velocity field. As shown in Figure 8, for low  $Ra$  the strain and the velocity field resemble that of the double-gyre as the similarities in velocity and velocity

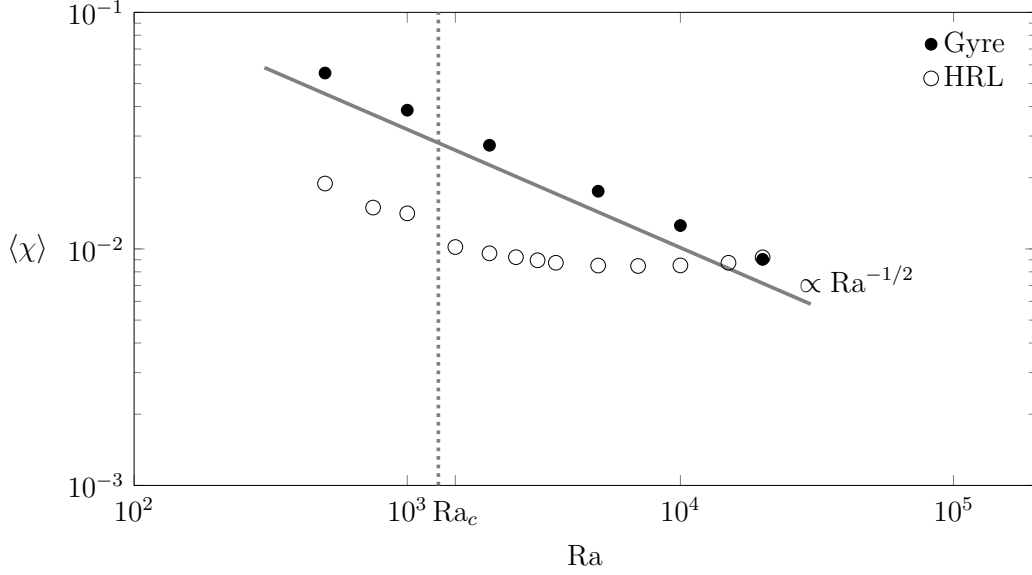


Figure 9: Dependence of the global scalar dissipation rate with the Rayleigh number for the double gyre system and the Horton-Rogers-Lapwood (HRL) problem. Mixing for HRL problem changes its behavior from uncoupled ( $\propto Ra^{-1/2}$ ) to convective around the critical Rayleigh number. This behavior has also been observed by Otero et al. (2004) and Hewitt et al. (2012).

autocorrelation indicate. The velocity structure is dominated by the convection pattern, which depends on the size and aspect ratio of the domain. Therefore the velocity changes happen in the scale of the domain size, as in the double-gyre case, and the compression rate is independent of  $Ra$ . In the convection dominated regime, however, the size of the domain becomes unimportant because the mixing process happens at the scale of the interface, which is of the order of the Batchelor scale. Velocity changes across a distance of the order of  $s_B$  and  $\gamma$  grows linearly with  $Ra$ . That is, compression and diffusion become coupled.

This change in behavior is reflected in the correlation length in the horizontal direction of the velocity and the strain. The correlation length depends on the number of convection cells for  $Ra < Ra_c$ . When a new cell is created as happens between  $Ra = 750$  (2 cells, see Figure 8) and  $Ra = 1000$  (3 cells) the correlation length decreases (Figure 10). It increases again when  $Ra = 1500$  and the system has two cells again. For  $Ra > Ra_c$  the correlation lengths decrease rapidly, indicating the transition to the convective dominated regime.

The interface compression model (8)–(13) explains the observed behaviors of  $\langle \chi \rangle$  in the different regimes based on the scalings of the compression rate  $\gamma$ . Regardless of the regime, the difference in concentration across the interface at the steady state is the one between the boundaries, that is  $c_b = 0$ . The effective length  $\omega_e$  associated to the stagnation points during first regime is weakly dependent on  $Ra$  because it is linked to the number of convection cells, which oscillates between 2 and 3 (Figure 8). The compression rate is, as explained before independent of  $Ra$ . Therefore from (10) and (13) we obtain  $s_B, \langle \chi \rangle \propto Ra^{-1/2}$ .

During the convection dominated regime velocity changes sharply across the interface thickness,

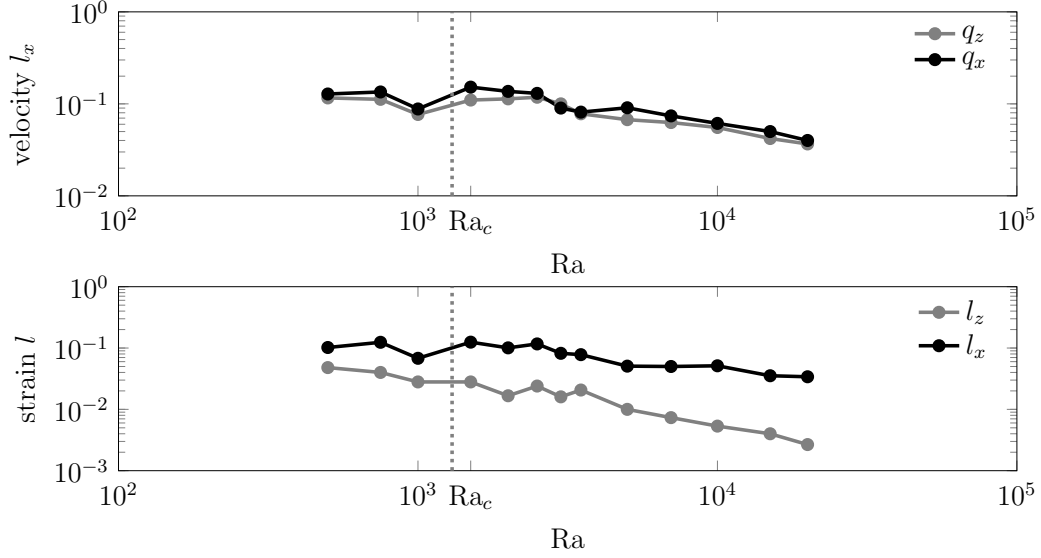


Figure 10: Horton-Rogers-Lapwood problem velocity correlation length in the horizontal direction for both components of the velocity (top) and strain correlation length in both directions. The correlation length is computed using the averaged magnitudes from  $t = 20$  to  $t = 100$ .

$\gamma \sim 1/s_B$  and (10) yields  $s_B \sim \text{Ra}^{-1}$ . The effective length  $\omega_e$  is independent of  $\text{Ra}$  because it is proportional to the number of stagnation points ( $\sim \text{Ra}$ ) times their individual effective length, which is proportional to the wavelength of the most unstable mode ( $\sim \text{Ra}^{-1}$ ) (Riaz et al., 2006; Hidalgo et al., 2015). Therefore from (13) we obtain  $\langle \chi \rangle \sim \text{Ra}^0$ .

Numerical simulations confirm the former analysis. As in the double-gyre case, we define the interface width as the square root of the second central moment of  $c(1-c)$ . We compute the second central moment at all locations along the top boundary and take as representative the interface width the minimum measured value since the movement along the boundary of the stagnation point and the alternation of places where the interface is compressed leads to an time average that overestimates the interface width. We observe (Figure 11) that there is a change in the scaling of the interface width around  $\text{Ra}_c$  from a value close to the  $\text{Ra}^{-1/2}$  predicted by the model to a  $\text{Ra}^{-1}$  value virtually equal to the model prediction and the observations in previous works Rees et al. (2008); Hidalgo and Carrera (2009); Slim and Ramakrishnan (2010); Hewitt et al. (2013a).

### 5.3 Mixing state

Similarly to the double-gyre case the increasing strength of convection narrows the concentration pdf around the average concentration of  $c = 0.5$  (Figure 12 left). However,  $p(c)$  is not as sharp as in the double-gyre case because the area between the convection cells or columnar plumes where the fluid is well-mixed are smaller. This area grows as  $\text{Ra}$  increases, which leads to a smaller concentration variance (Figure 12 right) and a more homogeneous system.

Contrary to the scalar dissipation rate  $\langle \chi \rangle$ , which is dominated by the concentration gradients at the interface, the mixing state of the system does not become independent of  $\text{Ra}$  as the system passes

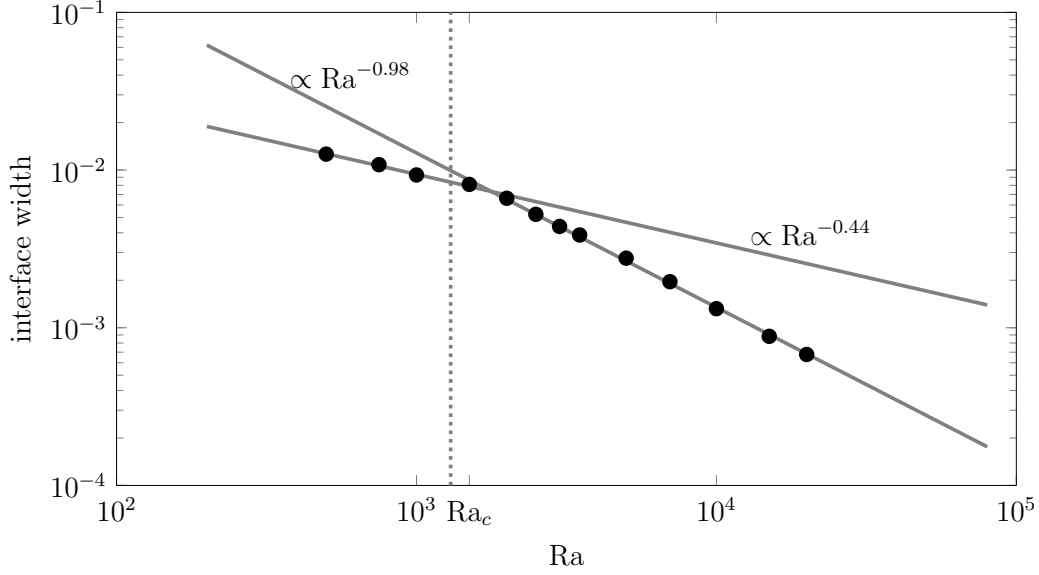


Figure 11: Interface width dependence on  $Ra$  for the Horton-Rogers-Lapwood problem. The width is computed using the average concentration from  $t = 20$  to  $t = 100$  and it is as the square root of the minimum second central moment of  $c(c - 1)$  along the  $x$  direction.

to the chaotic convection regime. The decrease in mixing efficiency happens around  $Ra \approx 10000$ , which is one order of magnitude bigger than  $Ra_c$ .

The dependence of  $\sigma_c^2$  on  $Ra$  implies an in principle counter-intuitive behavior: mixing increases with reducing diffusion. The responsible for this behavior is the increasingly chaotic convection, which stirs the system below the interface more efficiently than the convection cells, and leads together with a decreasing but finite diffusion to a more efficient homogenization of the mixture.

## 6 Stagnation points at mobile interfaces

In stratified fluid systems the interface between the fluids is not stationary and in general does not remain flat (Hewitt et al., 2013a). We relax now the assumption of a fixed flat interface and analyze a system subject to a Rayleigh-Taylor instability triggered by an unstable stratification of fluids. The interface compression and mixing model for this system was previously developed by Hidalgo et al. (2015), which we further discuss below.

### 6.1 Rayleigh-Taylor instability

We consider a rectangular domain of length 1 and height 2 with top and bottom impervious boundaries and periodic boundary conditions on the sides (Figure 13). Initially the system is in equilibrium with a less dense fluid on top of a dense one with the interface located at  $z = 1$ . The fluids are fully miscible. Instabilities are triggered by a fluid non-linear non-monotonic density law based on the mixtures of propylene-glycol and water (Backhaus et al., 2011; Dow Chemical, 2011) which is

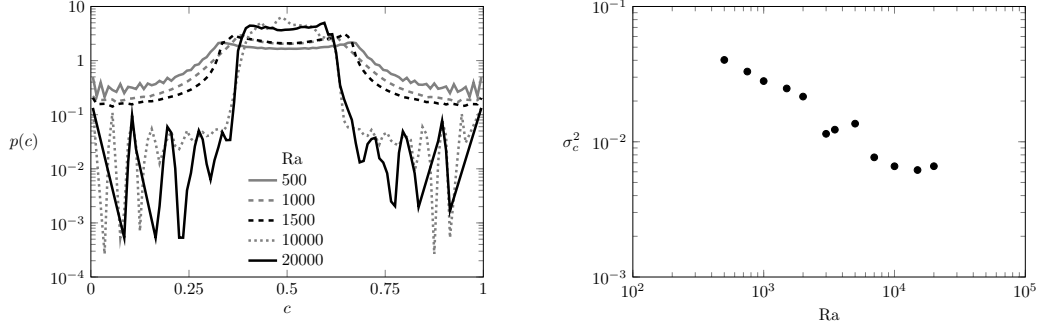


Figure 12: Probability density function of the time averaged concentration for the HRL problem (left) and pdf variance (right). Concentration was averaged from  $t = 20$  to  $t = 100$ . Colors indicate different Ra. For high Ra the pdf display some noise for the extrem values of concentration.

approximated in dimensionless form by  $\rho(c) = 6.19c^3 - 17.86c^2 + 8.07c$  (Hidalgo et al., 2015). Note that the dimensionless density is zero for  $c = 0$  (bottom fluid) and negative for  $c = 1$  (top fluid). The maximum density is found at  $c_m = 0.26$  so that the mixture of the fluids is denser than any of the pure ones (Neufeld et al., 2010; Hidalgo et al., 2012, 2015). Again, the system is completely characterized by the Rayleigh number (4) defined with  $q_c = k\Delta\rho g H_0/\mu$ , where  $\Delta\rho$  is the density difference between the maximum and the bottom fluid, and  $L_c = H_0$  is the initial position of the interface.

## 6.2 Interface compression and and scalar dissipation

The global scalar dissipation rate (Figure 14) shows that there are three main regimes: diffusive, convection dominated, and convection shutdown. At the beginning the fluids mix diffusively until the increase of density at the interface creates instabilities that lead to a convection dominated regime. The convection dominated regime is characterized by a constant global scalar dissipation rate, and the formation of fingering patterns. As the fluids mix and the concentration difference between the fluids diminishes, convection and mixing slow down.

As in the previous problems, mixing is related to the interface and velocity structure evolution. The main difference with the double-gyre and the HRL problems is that the interface between the fluids is not at rest as can be seen in the concentration maps in Figure 13. As the top fluid dissolves in the bottom fluid the interface moves up. Figure 15 (left) shows the velocity of the interface computed from  $c(1 - c)$  as illustrated in the center and right panels of the same figure. The maximum speed is observed during the convection dominated regime after which the interface velocity decreases.

The compression rate  $\gamma$  is given by the net velocity change across the interface as

$$\gamma = \frac{q_b - q_i}{s}, \quad (18)$$

where  $q_b$  is the velocity of the up-welling fluid and  $q_i$  is the interface velocity at the stagnation point. The up-welling fluid moves with a velocity proportional to the difference with respect to the

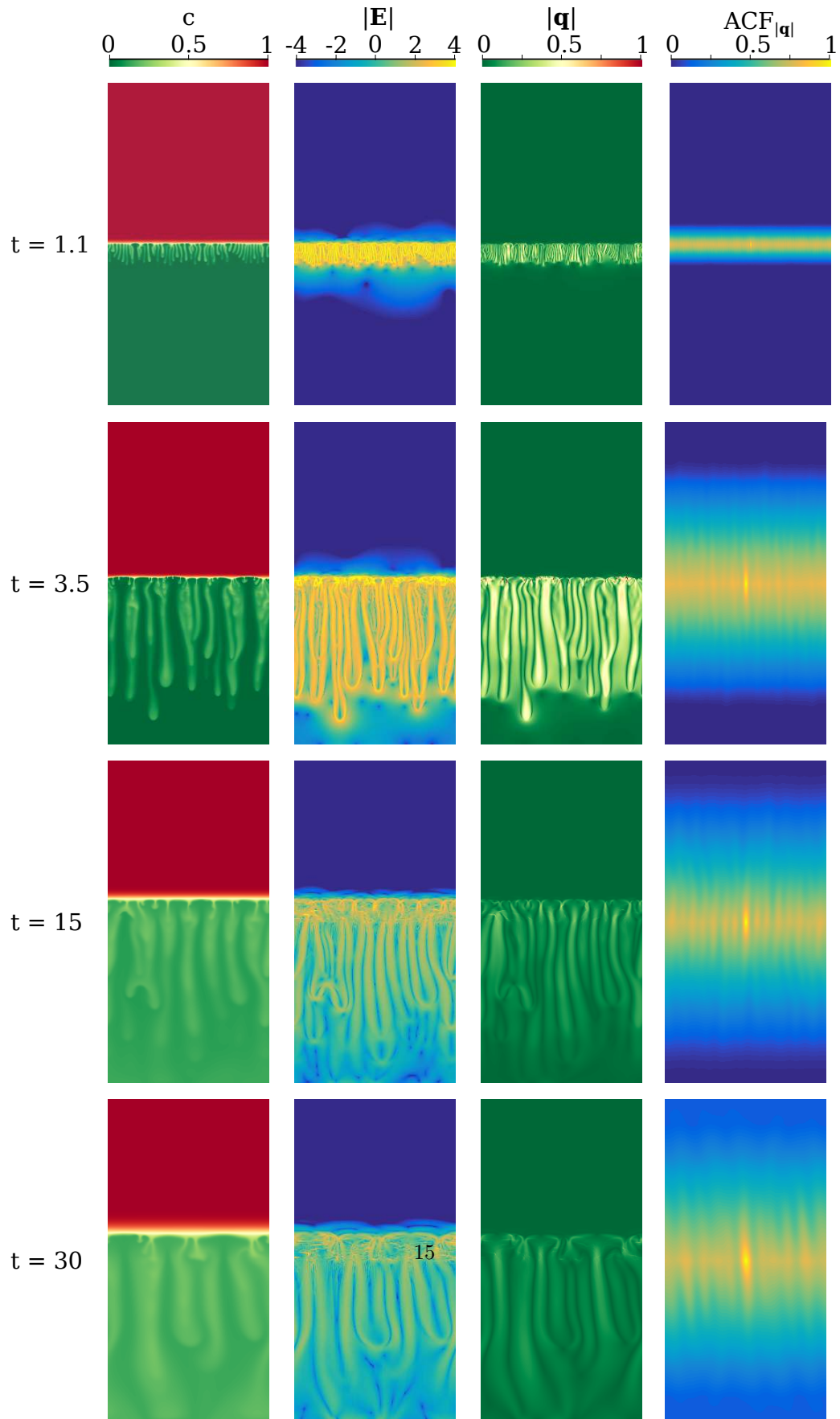


Figure 13: From left to right: concentration, determinant of the strain tensor  $\mathbf{E}$ , modulus of the velocity, and 2D normalized autocorrelation of the velocity field for the two-fluid system under a

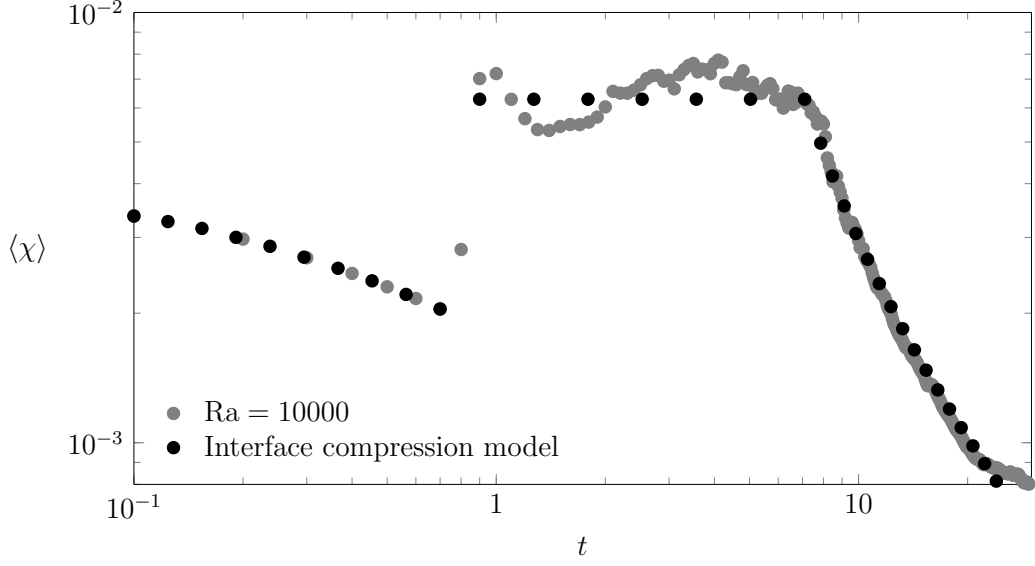


Figure 14: Evolution with time of the global scalar dissipation rate for the two-fluid with  $Ra = 10000$  for the numerical simulation (dots) and the interface compression model (solid line).

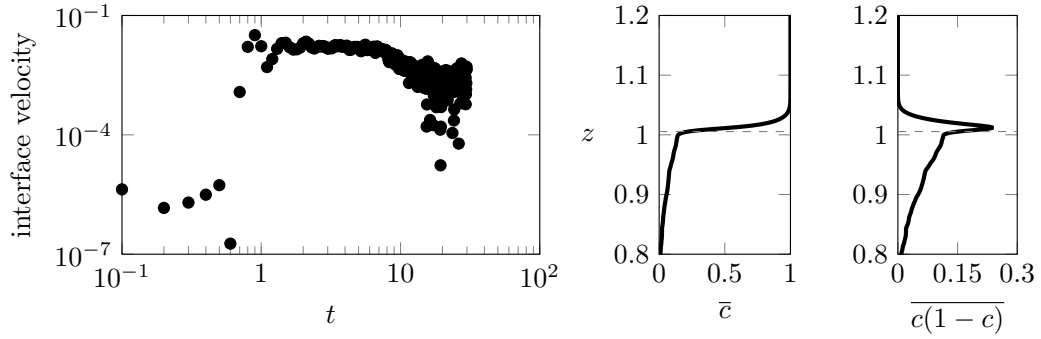


Figure 15: Interface velocity for the two-fluid system with  $Ra = 10000$  (left). Overlines indicate horizontally averaged magnitudes. The interface position is determined as first zero of the derivative of  $\overline{c(1-c)}$  with respect to  $z$  after the maximum. This is illustrated on the plots on the right where the  $\bar{c}$  and  $\overline{c(1-c)}$  are plotted for  $t = 1.4$ ,  $Ra = 10000$ . The position of the interface is indicated by the black dashed line.



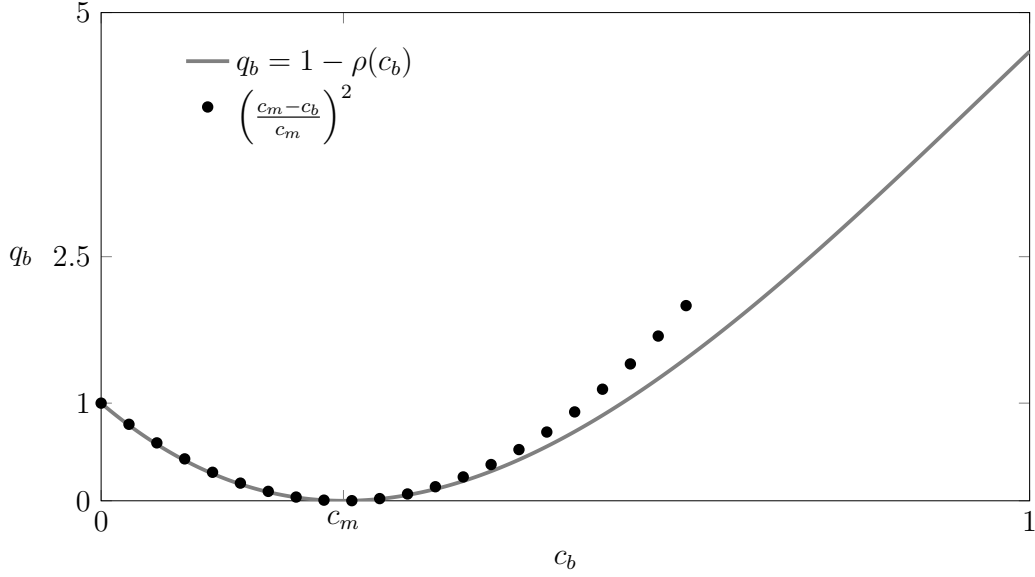


Figure 16:  $\Delta\rho(c_b) = 1 - \rho(c_b)$  (solid line) can be approximated by  $((c_m - c_b)/c_m)^2$  (dots). For the simulations in this study  $c_m = 0.26$ .

maximum density. For the chosen density law and  $c_b < c_m$   $q_b$  can be approximated by (Figure 16)

$$q_b(c_b) = \left( \frac{c_m - c_b}{c_m} \right)^2, \quad (19)$$

where, we recall,  $c_b$  is the average concentration below the interface and  $c_m$  the concentration for which density is maximum.

The velocity of the interface at the stagnation point is proportional to the dissolution flux, therefore

$$q_i = \frac{1 - c_b}{s\text{Ra}}, \quad (20)$$

and the compression rate can be written as

$$\gamma = \frac{1}{s} \left( q_b - \frac{1 - c_b}{s\text{Ra}} \right). \quad (21)$$

Then the steady state solution of (8) is approximated by (see Hidalgo et al., 2015)

$$s \approx \frac{2 - c_b}{(1 - c_b)^2 \text{Ra}}. \quad (22)$$

Equations (21) and (22) show that the fact that the interface motion leads to a lower compression of the interface and smaller dissolution flux across it than in the HRL problem. The difference in the dissolution flux between fixed and moving interfaces was noted by Hidalgo et al. (2012).

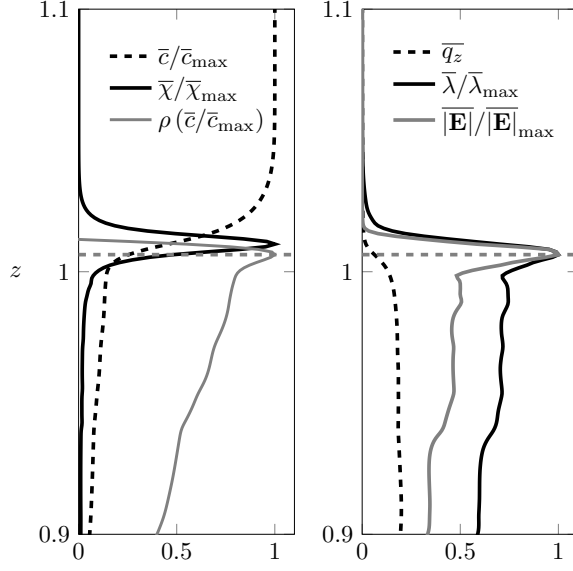


Figure 17: Horizontally averaged concentration, scalar dissipation rate and density (left), and vertical component of the velocity, determinant of the strain tensor  $\mathbf{E}$ , and its maximum eigenvalue  $\lambda$ . Some magnitudes are normalized by their maximum value. Maximum mixing is found above the location of maximum compression (dashed line). Data correspond to the  $Ra = 10000$  case for  $t = 1.4$ .

Maximum compression and scalar dissipation rate  $\chi$  happen at the interface where the maximum strain is also found (Figure 13). There is also a high strain on the sides of the fingers, however, their contribution to mixing is small because the concentration difference between the finger center and the surrounding fluid is low. Moreover, the increasing width of the fingers softens the concentration gradient therefore reducing even more their contribution to the mixing as time passes. The close relation between velocity, mixing, and strain is illustrated in Figure 17. The maximum strain, indicated by the determinant of the strain tensor and the maximum of its eigenvalues, occurs at the same height as the maximum density. At this position the derivative of  $q_z$  is maximum too. Maximum scalar dissipation rate however, is found a little above that point. This is caused by the non-linear density law, which makes the interface asymmetric as it is compressed only from the bottom. The interface asymmetry is more severe in the HRL and double-gyre and problems because of static the boundary (see Figure 3).

When convection dominates, the up-welling fluid is still the initial one, therefore  $c_b = 0$  and  $q_b = 1$ . As a result the interface compression is maximum (Figure 19). Using (22) and (13) leads to

$$s_B = \frac{2}{Ra} \quad (23)$$

and

$$\langle \chi \rangle = \frac{\omega_e}{4\sqrt{\pi}}, \quad (24)$$

where  $\omega_e \propto n_{sp} s_B$  with  $n_{sp}$  the number of stagnation points. At the onset of the instability, the fingers distribute according to the wavelength  $\lambda_c$  of the most unstable mode. Therefore the  $n_{sp}$  can be estimated using the results of Riaz et al. (2006) as  $n_{sp} = 1/\lambda_c = (\beta_c \text{Ra})/(2\pi)$ , which yields  $\omega_e = \beta_c \pi$ . Finally,

$$\langle \chi \rangle = \frac{2}{\pi^{3/4}} \beta_c, \quad (25)$$

which is independent of Ra because of the equilibrium between the diffusive interface expansion and the compression exerted by the buoyant fluid. Hidalgo et al. (2015) obtained  $\beta_c = 0.018$  from their simulations, which is  $c_m$  times the one reported by Riaz et al. (2006) for a linear density law with  $c_m = 1$ . Therefore the shape of the density law plays a critical role not only in the location of the maximum compression (Figure 17) but also on the value of the scalar dissipation rate during convection.

As the concentration of the bottom fluid increases the interface compression and convection weaken and the interface width grows rapidly as can be seen comparing figures 18 and 19 in which the increase in  $c_b$  happens at the same time in which the interface width grows. The  $1 - c_b \sim t^{-1/4}$  behavior in Figure 18 is in good agreement with the results of Hidalgo et al. (2015)

$$c_b = 1 - [1 + 2\omega_e(t - \tau_s)]^{-1/4} \quad (26)$$

which reproduces well the behavior of  $\langle \chi \rangle$  during the convection shutdown regime (see Figure 14). In equation (26)  $\tau_s$  is the time when convection shutdown begins and the effective length behaves as  $\omega_e \propto 0.002\sqrt{\text{Ra}}$  reflecting that the Rayleigh number becomes meaningful again when the fingers reach the bottom of the system. From that moment on velocity field is again influenced by the domain size and the wide fingers behave similarly to the convection cells of the HRL problem.

As the regimes succeed each other, the structure of the velocity field changes (Figure 13). The maximum velocity is found during the convection dominated regime and decreases as convection shuts down. The velocity autocorrelation  $\text{ACF}_{|\mathbf{q}|}$  (Figure 13 right column) reflects the horizontal structure of the fingering pattern with a decreasing number of local maxima as fingers coarsen. During the convection dominated regime the velocity and its autocorrelation are similar to the high Ra HRL problem (compare Ra = 10000 in Figure 8 to  $t = 3.5$  in Figure 13). During convection shutdown after the fingers hit the bottom of the domain the velocity structure resembles that of the low Ra HRL problem because the fingering patterns are similar to elongated convection cells (compare Ra = 750, 1000 in Figure 8 to  $t = 30$  in Figure 13).

The velocity and strain correlation lengths also evolve during the three regimes (Figure 20). The velocity correlation length in both directions is minimum before the onset of convection after which the maximum velocity is found. Then, the velocity correlation length reflects the creation of the fingering pattern. While the correlation length of  $q_z$  grows and stabilizes around a constant value, the correlation length of  $q_x$  continues growing as new fingers form and merge. A similar behavior is observed for the correlation length of the strain. Its correlation length in horizontal direction follows that of the horizontal velocity. In the vertical direction, however, the maximum correlation length is found after the onset of convection. This is caused by the growing fingers along which there is a high strain. At late times it decreases as the strain along the fingers becomes weaker.

### 6.3 Mixing state

The mixing state of the system also changes with the different regimes. In the beginning the system mixes slowly by diffusion and the concentration pdf has two distinct peaks at the extreme concen-

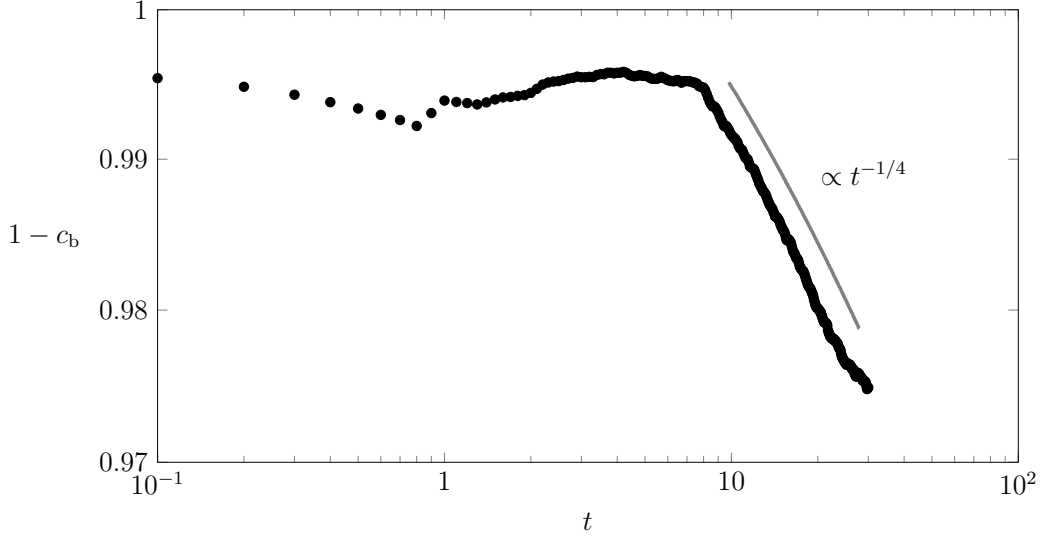


Figure 18: Evolution of the average concentration below the interface for the two-fluids system ( $Ra = 10000$ ). The concentration  $c_b$  is constant during the convection dominated regime and decreases as  $t^{-1/4}$  during convection shutdown.

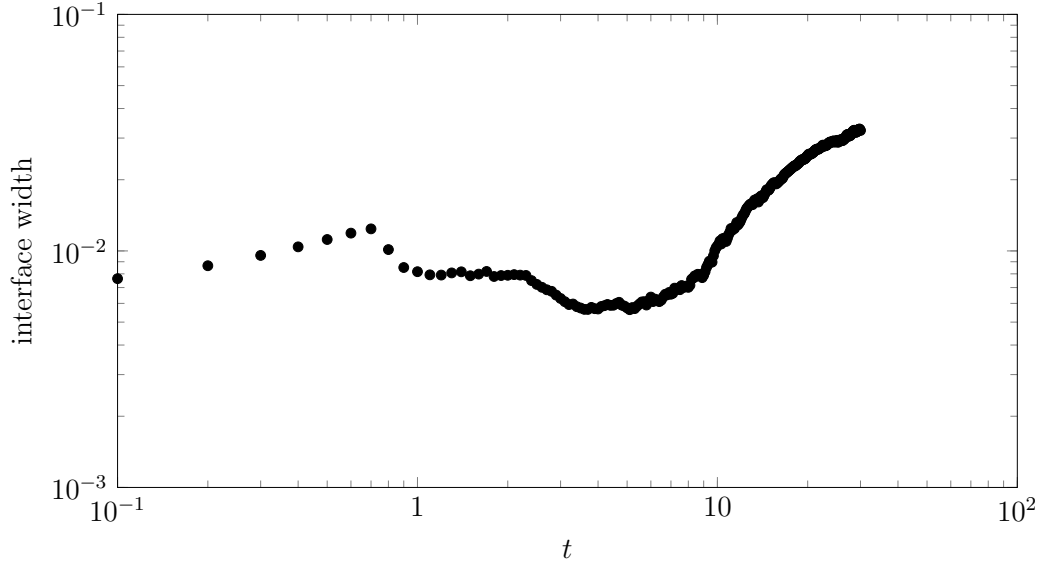


Figure 19: Interface width for the two fluids system ( $Ra = 10000$ ). The interface width is defined as the square root of the second moment of the horizontal average of  $c(1 - c)$ . This value follows the expected temporal evolution but overestimates the value of the interface width because of the influence of the fingers (see Figure 15).

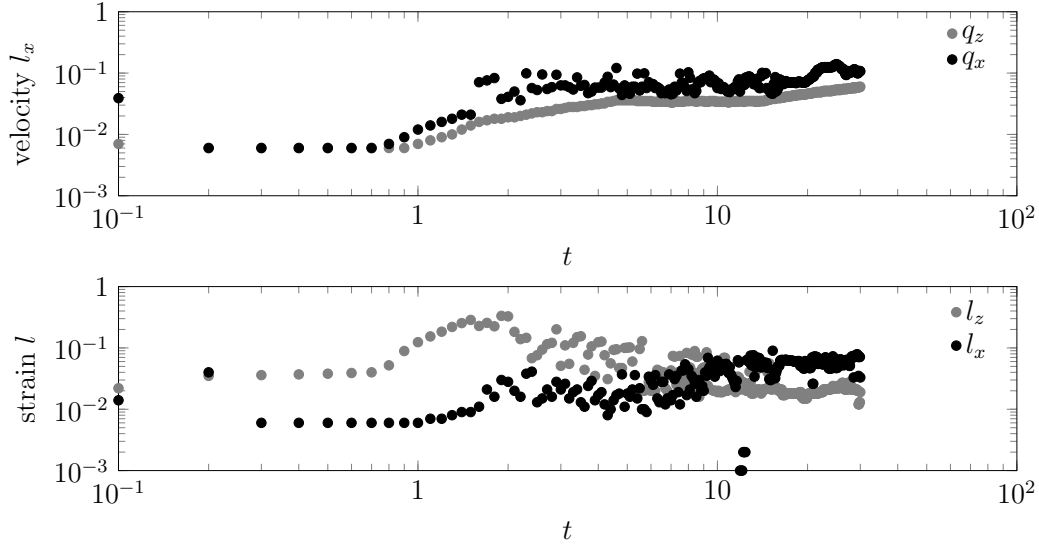


Figure 20: Evolution with time of the velocity correlation length in the horizontal direction for both components of the velocity (top) and strain correlation length in both directions (bottom) for the two-fluid system with  $Ra = 10000$ .

trations (Figure 21 left) has two distinct peaks at the extreme concentrations. When convection takes over, the peak around the low concentration shifts as a consequence of the mixing created by the fingers. The peak around maximum concentration is widened by the effect of diffusion. Eventually diffusion will take the system to a well-mixed state with uniform 0.5 concentration because the fluid occupied the same volume initially. However, there is an intermediate state of duration of the order of  $1/Ra$  characterized by a skewed concentration pdf displaying high probabilities around the concentration of the initial top fluid ( $c = 1$ ) and a peak near  $c_m$  as shown in Figure 21 (left) for  $t = 25$ .

In the two-fluid system there are no boundary dissolution fluxes, therefore,  $\langle \chi \rangle$  is proportional to the time derivative of the concentration variance. Figure 21 (right) shows how the system homogenization evolves in accordance with  $\langle \chi \rangle$ . Initially, the mixing state is given by the initial conditions. During the onset of the instabilities  $\sigma_c^2$  increases. However, it reduces as soon as they are fully developed. This shows that the chaotic convection that creates the fingering structures is an efficient mixing mechanism. As convection shuts down, the bottom fluid mean concentration approaches  $c_m$  for which density is maximum and the density stratification approaches to a stable configuration. Then convection weakens and the fingers merge and become wider, which makes the gradients of concentration at the interface and below smaller. In this regime the mixing efficiency decreases as well as the speed at which the system evolves towards the well-mixed state.

## 7 Conclusions

We have studied the mixing in porous media under unstable flow conditions using an interface compression model that is able to reproduce the observed dependency of the global scalar dissipation

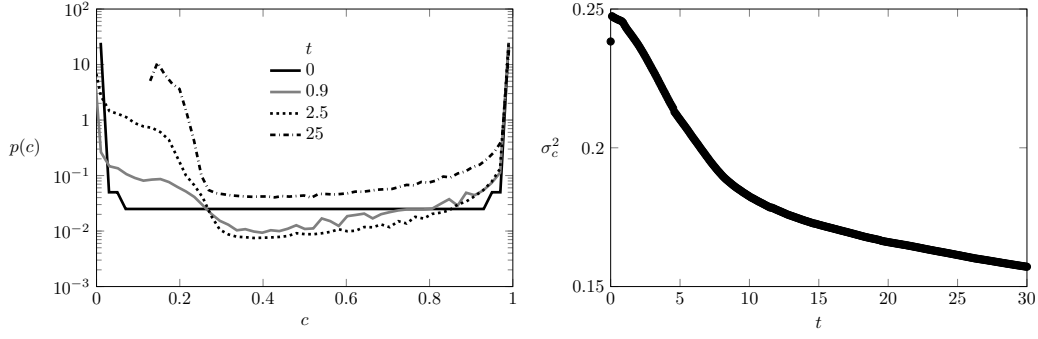


Figure 21: Concentration pdf for different times  $Ra = 10000$ .

rate  $\langle \chi \rangle$  (equivalent to the Nusselt number). The model, introduced through the analysis of a problem with a synthetic double-gyre velocity field, links the dissolution fluxes to the interface width. The width of the interface is modified by the velocity field, whose characteristics are related to the kind of instabilities and the concentration evolution.

The Horton-Rogers-Lapwood problem was used to study a Rayleigh-Bénard instability in which the fluid interface is immobile. The system displays two regimes. First, it organizes itself into convection cells as in the double-gyre. During this regime the velocity field is not independent of the domain size and the compression rate  $\gamma$  is independent of diffusion, which leads to  $\langle \chi \rangle \propto Ra^{-1/2}$ . Above  $Ra_c$ , the convection cells turn into columnar plumes. The velocity autocorrelation decreases abruptly and the system's size becomes irrelevant so that  $\gamma$  is of the order of  $1/s_B$ , therefore related to diffusion, and  $\langle \chi \rangle \propto Ra^0$ .

The case in which the interface is mobile was analyzed using a Rayleigh-Taylor instability in which the unstable density stratification was achieved by the mixture of two fluids with a non-monotonic density law. The system experiences three regimes. A diffusive regime in which the interface between the fluids grows. Then a convection dominated regime after the onset of the instabilities in which  $\langle \chi \rangle$  is independent of  $Ra$ . This behavior is similar to the high  $Ra$  HRL problem. The domain size does not affect the buoyancy fluxes and the interface width is controlled by a compression rate linked to the diffusion. Finally, a convection shutdown regime in which the system slowly approaches to a stable density stratification as the fluids mix. This regime is characterized by a temporal dependency of  $\langle \chi \rangle$ . The system then behaves as finite and the correlation length of the velocity grows.

The interface compression model and the analysis of the velocity field revealed that the scaling of  $\langle \chi \rangle$  is linked to the system size experienced by the velocity field. When the velocity field and concentration patterns are constrained by the domain boundaries,  $\chi \propto Ra^{-1/2}$ . However, when the structure of the velocity field breaks because of the strong convection the size of the domain becomes unimportant and  $\langle \chi \rangle$  independent of  $Ra$ .

We have shown that the global scalar dissipation  $\langle \chi \rangle$  is controlled by the dynamics of the fluid interface around the velocity field stagnation points. It is therefore expected that the stagnation points play an central role in the location and magnitude of mixing induced chemical reactions. The reaction hot spots will be preferentially found near the maximum dissolution (and maximum local scalar dissipation rate) takes place. The fingering and columnar patterns contribute much less to  $\langle \chi \rangle$ . However they are essential for the mixing state of the system.

The mixing state of the systems also depended on the nature of the instabilities. The variance of concentration decreases by the mixing of the convection patterns increases because of the fluxes through the boundaries. The double-gyre and HRL problems reach a steady mixing state in which both effects equilibrate and the variance of the concentration remains constant. In both cases convection makes the system more homogeneous. For low  $Ra$  the steady state is achieved earlier and the dissolution fluxes are bigger because they are proportional to  $Ra^{-1/2}$ . For high  $Ra$  the system is better mixed and displays a narrower concentration pdf but it takes it time to arrive to that state. The Rayleigh-Taylor instability lacks boundary fluxes. The evolution of the mixing state is governed by the scalar dissipation rate. During the period in which convection dominates mixing is maximum as well as the dissolution fluxes. As convection ceases the efficiency of the system to mix itself decreases. Therefore, the better mixed the system is the lower the dissolution fluxes. This suggest that a certain level of segregation might be desirable to maintain chemical reactions and fluxes through the boundary. Contrary to intuition, the best mixing state, i.e., lower variance of concentration, is attained for high  $Ra$ . That is a reduction in diffusion favors the homogenization of the concentration. This homogenization is achieved by the stirring created by the instability patterns.

J.J.H. and M.D. acknowledge the support of the European Research Council through the project MHetScale (FP7-IDEAS-ERC-617511). J.J.H. acknowledges the support of the Spanish Ministry of Economy and Competitiveness through the project Mec-MAT (CGL2016-80022-R).

## References

- Abarca, E., Carrera, J., Sánchez-Vila, X., and Voss, C. I. (2007). Quasi-horizontal circulation cells in 3d seawater intrusion. *Journal of Hydrology*, 339(3-4):118–129.
- Backhaus, S., Turitsyn, K., and Ecke, R. E. (2011). Convective instability and mass transport of diffusion layers in a Hele-Shaw geometry. *Phys. Rev. Lett.*, 106(10).
- Batchelor, G. K. (1959). Small-scale variation of convected quantities like temperature in turbulent fluid part 1. general discussion and the case of small conductivity. *Journal of Fluid Mechanics*, 5(1):113–133.
- Cheng, P. (1979). Heat transfer in geothermal systems. *Advances in Heat Transfer*, 14:1 – 105.
- Ching, E. S. C. and Lo, K. F. (2001). Heat transport by fluid flows with prescribed velocity fields. *Physical Review E*, 64(4).
- Cooper, H. H. (1964). Sea water in coastal aquifers. USGS Numbered Series 1613, USGS.
- De Simoni, M., Carrera, J., Sánchez-Vila, X., and Guadagnini, A. (2005). A procedure for the solution of multicomponent reactive transport problems. *Water Resour. Res.*, 41(11):W11410.
- Dentz, M., Le Borgne, T., Englert, A., and Bijeljic, B. (2011). Mixing, spreading and reaction in heterogenous media: a brief review. *J. Cont. Hydrol.*, 120-121:1–17.
- Dow Chemical (2011). Propylene glycols - density values. [https://dow-answer.custhelp.com/app/answers/detail/a\\_id/7471](https://dow-answer.custhelp.com/app/answers/detail/a_id/7471).

- Dyga, R. and Troniewski, L. (2015). Convective heat transfer for fluids passing through aluminum foams. *Archives of Thermodynamics*, 36(1):139–156.
- Elder, J. W. (1968). The unstable thermal interface. *Journal of Fluid Mechanics*, 32(01):69 – 96.
- Ennis-King, J. P. and Paterson, L. (2005). Role of convective mixing in the long-term storage of carbon dioxide in deep saline formations. *SPE Journal*, 10(03):349–356.
- Graham, M. D. and Steen, P. H. (1994). Plume formation and resonant bifurcations in porous-media convection. *Journal of Fluid Mechanics*, 272(-1):67.
- Hamadouche, A., Nebbali, R., Benahmed, H., Kouidri, A., and Bousri, A. (2016). Experimental investigation of convective heat transfer in an open-cell aluminum foams. *Experimental Thermal and Fluid Science*, 71:86–94.
- Hewitt, D. R., Neufeld, J. A., and Lister, J. R. (2012). Ultimate regime of high Rayleigh number convection in a porous medium. *Physical Review Letters*, 108(22).
- Hewitt, D. R., Neufeld, J. A., and Lister, J. R. (2013a). Convective shutdown in a porous medium at high Rayleigh number. *J. Fluid Mech.*, 719:551–586.
- Hewitt, D. R., Neufeld, J. A., and Lister, J. R. (2013b). Stability of columnar convection in a porous medium. *Journal of Fluid Mechanics*, 737:205231.
- Hidalgo, J. J. and Carrera, J. (2009). Effect of dispersion on the onset of convection during co<sub>2</sub> sequestration. *Journal of Fluid Mechanics*, 640:441–452.
- Hidalgo, J. J., Dentz, M., Cabeza, Y., and Carrera, J. (2015). Dissolution patterns and mixing dynamics in unstable reactive flow. *Geophysical Research Letters*, 42(15):63576364.
- Hidalgo, J. J., Fe, J., Cueto-Felgueroso, L., and Juanes, R. (2012). Scaling of convective mixing in porous media. *Phys. Rev. Lett.*, 109(26).
- Hidalgo, J. J., MacMinn, C. W., and Juanes, R. (2013). Dynamics of convective dissolution from a migrating current of carbon dioxide. *Ad. Water Resour.*, 62:511–519.
- Horton, C. W. and Rogers, F. T. (1945). Convection currents in a porous medium. *Journal of Applied Physics*, 16(6):367370.
- Howard, L. N. (1966). *Convection at high Rayleigh number*, pages 1109–1115. Springer Berlin Heidelberg, Berlin, Heidelberg.
- Kimura, S., Schubert, G., and Straus, J. M. (1986). Route to chaos in porous-medium thermal convection. *Journal of Fluid Mechanics*, 166(-1):305 – 324.
- Kitanidis, P. K. (1994). The concept of the dilution index. *Water Resour. Res.*, 30(7):2011–2026.
- Kueper, B. H. and Frind, E. O. (1991). Two-phase flow in heterogeneous porous media: 1. model development. *Water Resources Research*, 27(6):1049–1057.
- Lapwood, E. R. (1948). Convection of a fluid in a porous medium. *Mathematical Proceedings of the Cambridge Philosophical Society*, 44(04):508.



- Le Borgne, T., Dentz, M., Bolster, D., Carrera, J., de Dreuzy, J.-R., and Davy, P. (2010). Non-fickian mixing: Temporal evolution of the scalar dissipation rate in heterogeneous porous media. *Ad. Water Resour.*, 33(12):1468–1475.
- Le Borgne, T., Dentz, M., and Villerraux, E. (2013). Stretching, coalescence, and mixing in porous media. *Phys. Rev. Lett.*, 110(20).
- Le Borgne, T., Dentz, M., and Villerraux, E. (2015). The lamellar description of mixing in porous media. *J. Fluid Mech.*, 770:458–498.
- Martin, D., Griffiths, R. W., and Campbell, I. H. (1987). Compositional and thermal convection in magma chambers. *Contributions to Mineralogy and Petrology*, 96(4):465–475.
- Musgrave, D. L. (1985). A numerical study of the roles of subgyre-scale mixing and the western boundary current on homogenization of a passive tracer. *Journal of Geophysical Research: Oceans*, 90(C4):7037–7043.
- Neufeld, J. A., Hesse, M. A., Riaz, A., Hallworth, M. A., Tchelepi, H. A., and Huppert, H. E. (2010). Convective dissolution of carbon dioxide in saline aquifers. *Geophys. Res. Lett.*, 37(22):L22404.
- Otero, J., Dontcheva, L. A., Johnston, H., Worthing, R. A., Kurganov, A., Petrova, G., and Doering, C. R. (2004). High-Rayleigh-number convection in a fluid-saturated porous layer. *Journal of Fluid Mechanics*, 500:263281.
- Ottino, J. (1989). *The Kinematics of Mixing: Stretching, Chaos, and Transport*. Cambridge Texts in Applied Mathematics. Cambridge University Press.
- Ranz, W. E. (1979). Applications of a stretch model to mixing, diffusion, and reaction in laminar and turbulent flows. *AIChE J.*, 25(1):41–47.
- Rees, D., Selim, A., and Ennis-King, J. (2008). The instability of unsteady boundary layers in porous media. In Vadasz, P., editor, *Emerging Topics in Heat and Mass Transfer in Porous Media. From Bioengineering and Microelectronics to Nanotechnology*, volume 22 of *Theory and Applications of Transport in Porous Media*, pages 85–110. Springer, Netherlands.
- Riaz, A., Hesse, M., Tchelepi, H. A., and Orr Jr., F. M. (2006). Onset of convection in a gravitationally unstable diffusive boundary layer in porous media. *J. Fluid Mech.*, 548:87–111.
- Sanford, W. E., Whitaker, F. F., Smart, P. L., and Jones, G. (1998). Numerical analysis of seawater circulation in carbonate platforms: I, geothermal convection. *American Journal of Science*, 298(10):801–828.
- Shadden, S. C., Lekien, F., and Marsden, J. E. (2005). Definition and properties of lagrangian coherent structures from finite-time Lyapunov exponents in two-dimensional aperiodic flows. *Physica D: Nonlinear Phenomena*, 212(3-4):271304.
- Slim, A. C. (2014). Solutal-convection regimes in a two-dimensional porous medium. *Journal of Fluid Mechanics*, 741:461491.
- Slim, A. C. and Ramakrishnan, T. S. (2010). Onset and cessation of time-dependent, dissolution-driven convection in porous media. *Physics of Fluids*, 22(12):124103.

- Szulczewski, M. L., Hesse, M. A., and Juanes, R. (2013). Carbon dioxide dissolution in structural and stratigraphic traps. *Journal of Fluid Mechanics*, 736:287–315.
- Tait, S. and Jaupart, C. (1989). Compositional convection in viscous melts. *Nature*, 338(6216):571–574.
- Villermaux, E. (2012). Mixing by porous media. *C. R. Mecanique*, 340(11-12):933–943.
- Villermaux, E. and Duplat, J. (2006). Coarse grained scale of turbulent mixtures. *Phys. Rev. Lett.*, 97:144506.
- Wells, A. J., Wettlaufer, J. S., and Orszag, S. A. (2011). Brine fluxes from growing sea ice. *Geophysical Research Letters*, 38(4). L04501.